



Stand-off trapping and manipulation of sub-10 nm objects and biomolecules using opto-thermo-electrohydrodynamic tweezers

Chuchuan Hong^{1,2}, Sen Yang^{1,3} and Justus C. Ndukaife^{1,2}

Optical tweezers have emerged as a powerful tool for the non-invasive trapping and manipulation of colloidal particles and biological cells^{1,2}. However, the diffraction limit precludes the low-power trapping of nanometre-scale objects. Substantially increasing the laser power can provide enough trapping potential depth to trap nanoscale objects. Unfortunately, the substantial optical intensity required causes photo-toxicity and thermal stress in the trapped biological specimens³. Low-power near-field nano-optical tweezers comprising plasmonic nanoantennas and photonic crystal cavities have been explored for stable nanoscale object trapping^{4–13}. However, the demonstrated approaches still require that the object is trapped at the high-light-intensity region. We report a new kind of optically controlled nanotweezers, called opto-thermo-electrohydrodynamic tweezers, that enable the trapping and dynamic manipulation of nanometre-scale objects at locations that are several micrometres away from the high-intensity laser focus. At the trapping locations, the nanoscale objects experience both negligible photothermal heating and light intensity. Opto-thermo-electrohydrodynamic tweezers employ a finite array of plasmonic nanoholes illuminated with light and an applied a.c. electric field to create the spatially varying electrohydrodynamic potential that can rapidly trap sub-10 nm biomolecules at femtomolar concentrations on demand. This non-invasive optical nanotweezing approach is expected to open new opportunities in nanoscience and life science by offering an unprecedented level of control of nano-sized objects, including photo-sensitive biological molecules.

Our present work capitalizes on the latest advances in electro-thermoplasmonic (ETP) trapping^{14–16} where ETP flow^{17,18} is used to initiate rapid particle transport towards a plasmonic hot spot for particle trapping at the hotspot. Opto-thermo-electrohydrodynamic tweezers (OTET), on the other hand, exploit the interaction between ETP flow and a.c. electro-osmotic flow to establish an electrohydrodynamic potential capable of low-power trapping and manipulation of sub-10 nm particles and biomolecules at tunable trapping locations that are several micrometres away from the high-intensity light spot. Our finding represents an important development in the optical nanomanipulation field by addressing the important task of trapping sub-10 nm particles such as small protein molecules without the risk of photo-induced damage. OTET provide the means to keep a single sub-10 nm object in a solution for minutes, without the need to physically tether it. Prior reported attempts to trap

objects away from the laser focus using complex beam profiles such as Laguerre–Gaussian beams¹⁹ or a repulsive thermophoretic force induced by a moving laser spot and a feedback system²⁰ have been reported. However, these works have been limited to resonant metallic objects and much larger particles, respectively. Using OTET, we also demonstrated the size-selective trapping of nanoscale objects such as 20 nm dielectric beads from a solution containing 20 nm and 100 nm beads at trapping locations that are several micrometres away from the laser illumination.

The OTET platform comprises a finite array of plasmonic nanoholes illuminated with light and a perpendicularly applied a.c. electric field, which generate optically induced thermal gradients and distorted a.c. electric field lines near the nanohole array, respectively, as depicted in Fig. 1a. The coupling of the nanohole array with light results in highly localized and enhanced electromagnetic hot spots, as depicted in Fig. 1b, which promotes light absorption. The enhanced light absorption results in a temperature increase and thermal gradient in the fluid. The simulated temperature increase for an incident light intensity of $3 \times 10^9 \text{ W m}^{-2}$ is depicted in Fig. 1c. An a.c. electric field is applied perpendicular to the nanohole array across a fluid element. The topography of the nanohole array results in the distortion of the applied a.c. electric field to give rise to both normal and tangential a.c. electric field components. The component of the a.c. electric field in the tangential direction exerts Coulombic forces on the diffuse charges in the electrical double layer induced at the interface between the nanohole array and the fluid. This electric-field-induced motion of the diffuse charges gives rise to an electro-osmotic motion²¹ of the fluid and the suspended particles that is directed radially outward, as depicted in Fig. 1d,e. An ETP flow^{14,18,22} is also induced by the action of both the laser-induced heating of the fluid near the plasmonic nanohole array and the applied a.c. field, and results in a fluid vortex that is directed radially inward as depicted in Fig. 1d,e. These two opposing microfluidic flows create a stagnation zone, where the fluid velocity goes to zero, that defines the position where a particle is trapped, as depicted in Fig. 1d. Since the position of the stagnation zone is farther away from the location of the laser beam, the particle is trapped several micrometres away from the laser focus. The localization of the particle in the out-of-plane direction occurs because of the particle–surface interaction force, which arises from the interaction between the surface charge on the particle and its image charge²³ in the conducting plane. This ability to structure the microfluidic flow field with a plasmonic nanohole array provides an elegant approach to create designer flow fields to suppress the

¹Vanderbilt Institute of Nanoscale Science and Engineering, Vanderbilt University, Nashville, TN, USA. ²Department of Electrical Engineering and Computer Science, Vanderbilt University, Nashville, TN, USA. ³Interdisciplinary Materials Science and Engineering, Vanderbilt University, Nashville, TN, USA.

✉e-mail: justus.ndukaife@vanderbilt.edu

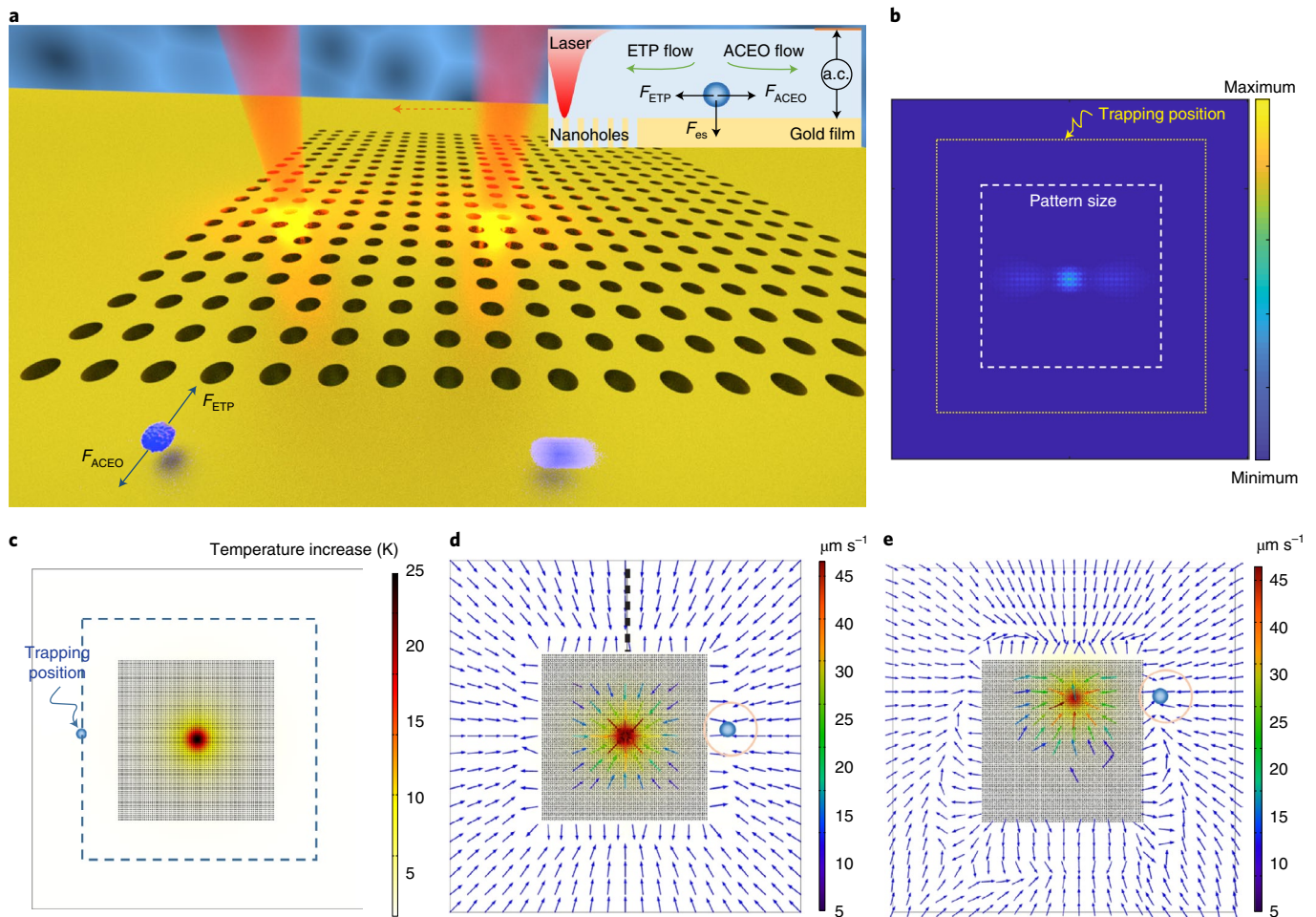


Fig. 1 Illustration and theoretical analysis of the OTET system. **a**, Illustration of the operating mechanism of the OTET system. By moving the laser on the plasmonic nanohole array, a single particle (blue sphere) is trapped away from the laser and follows the motion of the laser beam horizontally along the pattern edge. The inset shows the forces acting on a trapped particle when the laser and a.c. electric field is applied. ACEO, a.c. electro-osmotic flow; F_{ACEO} , the drag force from the a.c. electro-osmotic flow; F_{ETP} , the drag force from the ETP flow; F_{es} , the particle-surface interaction force. **b**, Electric field profile when a laser is focused at the centre of the nanohole array. At the trapping position, the electric field from the light is small enough to eliminate its influence on the trapped particle. **c**, Temperature profile at the surface of gold film when the laser is focused at the centre of the nanohole array. Particle trapping occurs several micrometres away from the maximum temperature region. **d**, Radial velocity vector plot near the surface when the laser is focused at the centre of the nanohole array. Particle trapping position is circled. The dashed line is explained in Fig. 4b. **e**, Radial velocity vector plot near the surface when the laser is focused off-centre. The particle trapping position changes due to the translation of the laser spot. The laser used in the simulation is a 973 nm Gaussian beam of 1 μm focus spot, with 3 mW power.

Brownian motion of particles and localize a single particle near a solid surface. If the laser illumination is displaced from the centre of the nanohole array pattern, the particle can be translated along the path defined by the topography of the nanohole array while still maintaining the distance dictated by the position of the stagnation zone as depicted in Fig. 1e. The physics of the electrohydrodynamic flows that enable trapping in OTET is described by several coupled partial differential equations, which we have solved numerically using the COMSOL Multiphysics software package, as shown in the Supplementary Information section.

The experimental demonstration of particle trapping and manipulation using OTET was carried out using an array of gold nanoholes with a diameter of 300 nm and a thickness of 120 nm, on a glass substrate. The fabrication was performed using a template stripping approach²⁴ (see Methods section). Experimental demonstration of trapping was performed using diluted solutions of fluorescently labelled bovine serum albumin (BSA) protein (see Methods section) with a hydrodynamic radius of 3.4 nm, as

well as 20-nm and 100-nm-diameter polystyrene beads. The BSA protein was diluted to a concentration of 15 fM. A linearly polarized laser beam with a wavelength of 973 nm was focused to a spot size of 1.33 μm on the nanohole array using a water-immersion objective lens with a numerical aperture (NA) of 1.2. Figure 2a (Supplementary Video 1) shows, frame by frame, the sequence of fast transport, trapping and release of a single BSA protein molecule. First, we illuminate the nanohole array (indicated by a red dot) with the laser light, and no macroscopic effect is apparent. Subsequently, an a.c. field of 83,333 V m^{-1} at a frequency of 10 kHz is applied across the channel, which results in the fast motion of the BSA protein molecule by the radially inward ETP flow towards the nanohole array; but no trapping occurs at this frequency. As the a.c. electric field frequency is reduced to 3 kHz, the opposing a.c. electro-osmotic flow causes the BSA protein molecule to be localized at a distance of approximately 8.6 μm from the edge of the nanohole array within 3 s. At this point, our system provides the freedom to select one of the following options: (1) keeping the BSA

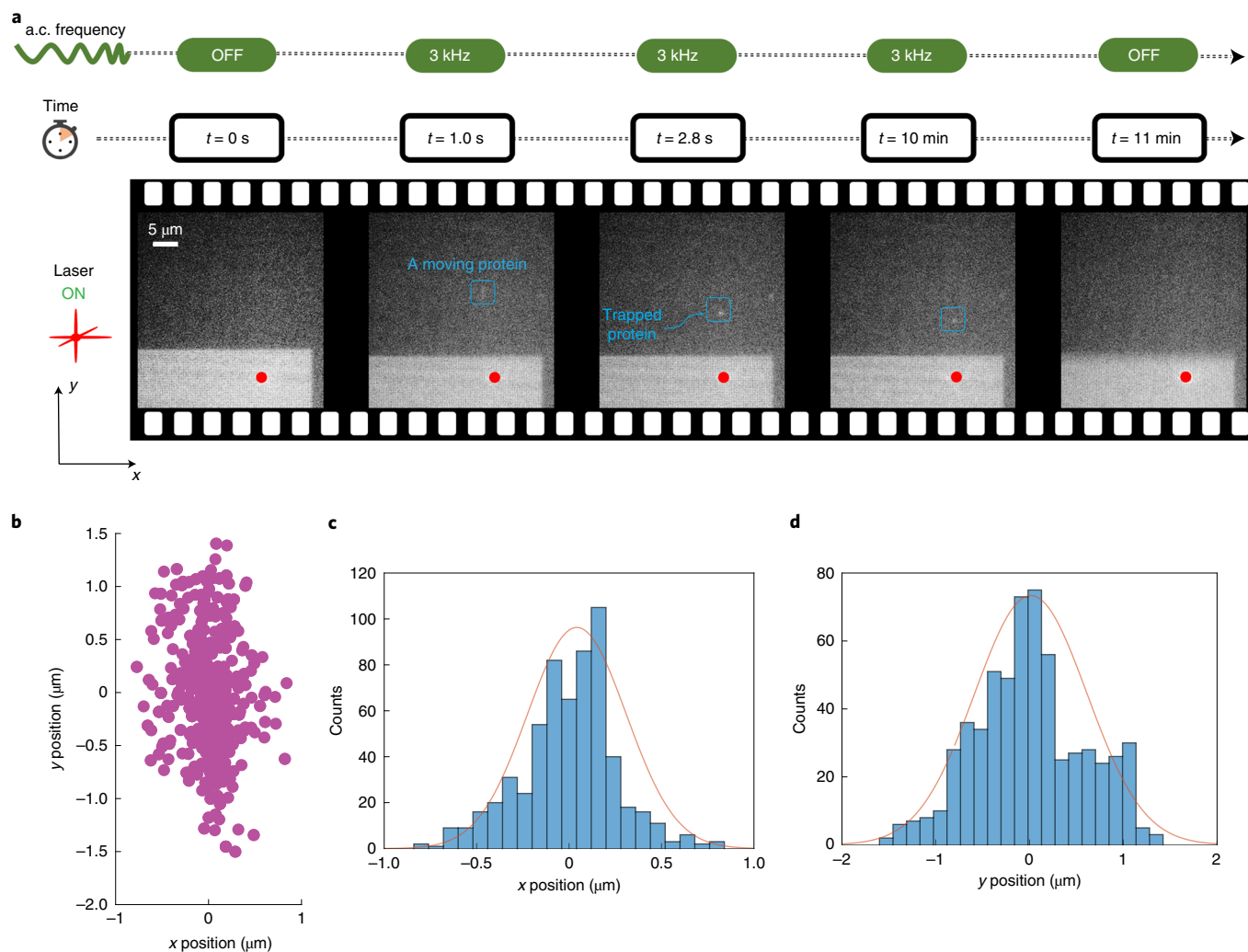


Fig. 2 | Demonstration of transport, trapping and release of a single BSA protein molecule, as well as the stability of a trapped single BSA molecule.

a. A frame-by-frame sequence of the rapid onset and long-lasting stable trap when a laser and an a.c. field are both applied. The red dot shows the laser position, and the single BSA molecule (the tiny bright dot) is highlighted in a blue rectangle. **b.** Transverse position (x - y) of a trapped single molecule. As shown in **a**, the x position is the position along the pattern's edge, and the y position is the position perpendicular to the pattern's edge. **c,d.** Histograms of lateral displacement along the x and y directions, respectively. The orange curve shows the Gaussian-shape fitted curve for clearer illustration.

molecule trapped using both the laser and a.c. field; (2) releasing the BSA protein by turning off the a.c. field; or (3) dynamically manipulating the BSA protein by moving the laser beam or translating the microscope stage. The last option represents another vital feature of OTET: enabling the dynamic manipulation of trapped sub-10 nm objects on-chip (Supplementary Video 2), which is not feasible in conventional chip-based plasmonic traps^{25,26} and geometry-induced electrostatic traps²⁷. Figure 2b shows the scatter plot of the trapped BSA's displacement. The BSA is more stably trapped along the x direction, that is, the direction perpendicular to the radial direction of the ETP and electro-osmotic flow field vectors.

The OTET exhibit a lower trapping stability along the y direction, which is the direction that aligns with the radial components of the opposing ETP and a.c. electro-osmotic flow velocity vectors. We attribute this to the fact that the radial components of the ETP and a.c. electro-osmotic flows exert drag forces on the particle along the y direction, which results in a lower trapping stability along this direction.

We also show that OTET possess a dynamic manipulation capability, as depicted in Fig. 3 and Supplementary Video 2. The trapped object is dynamically manipulated by translating the laser beam

across the nanohole array or moving the microscope stage. The motion of the object is along the edge that is parallel to the direction that the laser spot is moving relative to the nanohole array. An object that is trapped along the edge perpendicular to the direction of motion of the laser beam remains in position and not translated. Thus, in OTET, the trapped objects are not limited to a specific trapping location but can readily be transported to specific areas along topography defined by the nanohole array, while still maintaining a trapping location that is several micrometres away from the high-intensity laser focus.

The distance between the position of the trapped object and the edge of the nanohole array can be tuned by changing the a.c. field frequency, as depicted in Fig. 4a. At lower a.c. field frequency, the radially outward a.c. electro-osmotic flow is increased relative to the ETP flow, which causes the shifting of the stagnation zone radially outward. As the a.c. frequency is raised to 5 kHz, the trapping position of BSA protein is shifted inward to a location that is closer to the nanohole array. This observed trapping behaviour as a function of a.c. field frequency is also supported with numerical simulation. Figure 4b is a numerical simulation showing the location of the stagnation zone as a function of the a.c. field frequency.

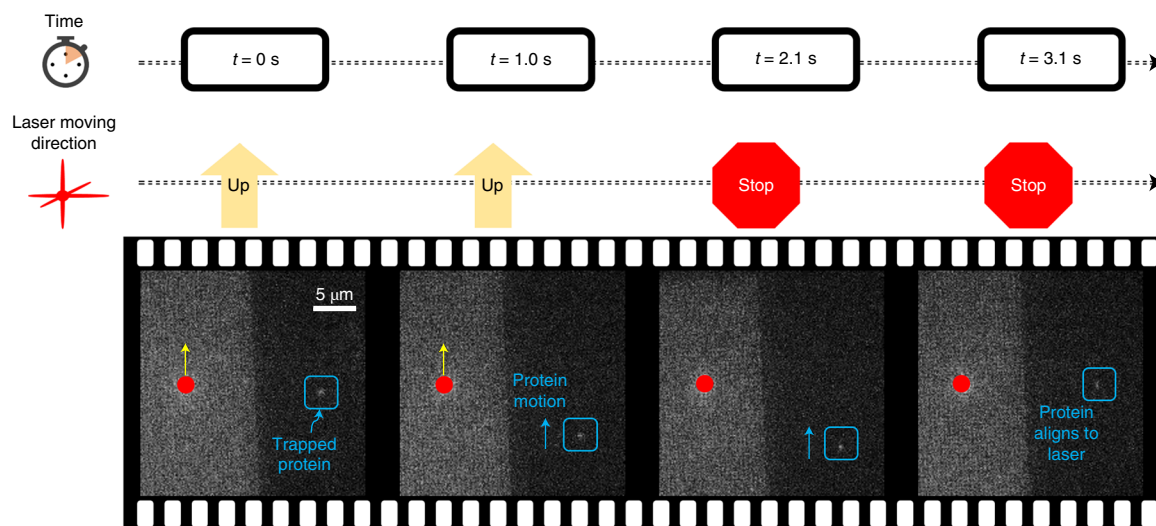


Fig. 3 | Frame-by-frame images showing a demonstration of dynamic manipulation of a single BSA protein molecule. Red dots show the laser spot position, and the single molecule (tiny bright dot) is highlighted inside a blue rectangle. Yellow arrows show the direction of laser motion, and the blue arrow indicates the molecule's motion. At the starting frame ($t = 0$ s), a single molecule is trapped close to the pattern's edge, and the laser starts to move relative to the nanohole array. During the laser motion (lasting 2.1 s), the single molecule follows the laser while maintaining a trapping location several micrometres away from the laser spot. The second frame is a typical moment captured at $t = 1.0$ s. At the moment when the laser stops moving, the single molecule keeps moving along the original direction and finally stops when it is aligned at the same level as the laser spot. These two steps are demonstrated in the third and fourth frames. Starting from $t = 3.1$ s, we move the laser in the opposite direction, downward, and the single molecule travels downward following the laser. The full video can be accessed in Supplementary Video 2.

The result indicates that the location of the stagnation zone, which defines the trapping location, increases with decreasing a.c. field frequency. Thus, by tuning the frequency of the applied a.c. field, the location of the trap away from the edge of the nanohole array can be controlled on demand.

The particle trapping stability in OTET can be controlled by tuning the a.c. field frequency. We observe that the particle–surface interaction force is generally stronger at lower a.c. field frequencies as depicted in Fig. 4a,b. This is attributed to the fact that for lower a.c. field frequencies, the electrical double layer surrounding the particle has sufficient time to be sufficiently polarized by the a.c. electric field.

The frequency dependence of the trapping stability can also be used for size-based sorting in OTET. Figure 5 shows the selective trapping of 20 nm polystyrene beads from a solution containing 100 nm and 20 nm beads. Initially, using an a.c. field frequency of 2.5 kHz, both 20 nm and 100 nm beads are trapped. When the frequency is increased to 4 kHz, the 100 nm beads are released from the trap, while the 20 nm beads remain in place. This feature could be harnessed for the sorting of exosomes, which range in size from 30 nm to 150 nm, from a population of extracellular vesicles, and represents an important application of OTET with great potential.

Conclusions

The ability to trap small biological molecules at femtomolar concentrations within a few seconds, along with their size-based sorting capability, makes OTET a promising tool for the biological sensing of analytes at low levels. The proposed nanomanipulation technique enables the immediate implementation of several exciting applications including (1) biological sensing at an ultra-low detection limit; (2) single-molecule analysis to determine the diffusion coefficient and electrokinetic mobility of proteins in solution; (3) the stabilization of single molecules within the observation volume for single-molecule Förster resonance energy transfer spectroscopy; and (4) size-based sorting of nanoscale objects, such as exosomes from a heterogeneous population of extracellular vesicles. With respect to

the last point, OTET feature a simple and fast lab-on-a-chip solution to the issue of capture and sorting of exosomes from a population of extracellular vesicles released by biological cells, which is crucial for single exosome analysis and for understanding the influence of cell heterogeneity on released exosomes for applications in drug delivery and diagnostics.

Online content

Any methods, additional references, Nature Research reporting summaries, source data, extended data, supplementary information, acknowledgements, peer review information; details of author contributions and competing interests; and statements of data and code availability are available at <https://doi.org/10.1038/s41565-020-0760-z>.

Received: 6 March 2020; Accepted: 30 July 2020;

Published online: 31 August 2020

References

1. Neuman, K. C. & Block, S. M. Optical trapping. *Rev. Sci. Instrum.* **75**, 2787–2809 (2004).
2. Ashkin, A. & Dziedzic, J. M. Optical trapping and manipulation of viruses and bacteria. *Science* **235**, 1517–1520 (1987).
3. Blázquez-Castro, A. Optical tweezers: phototoxicity and thermal stress in cells and biomolecules. *Micromachines* **10**, 507–549 (2019).
4. Juan, M. L., Gordon, R., Pang, Y., Eftekhari, F. & Quidant, R. Self-induced back-action optical trapping of dielectric nanoparticles. *Nat. Phys.* **5**, 915–919 (2009).
5. Pang, Y. & Gordon, R. Optical trapping of 12 nm dielectric spheres using double-nanoholes in a gold film. *Nano Lett.* **11**, 3763–3767 (2011).
6. Yoo, D. et al. Low-power optical trapping of nanoparticles and proteins with resonant coaxial nanoaperture using 10 nm gap. *Nano Lett.* **18**, 3637–3642 (2018).
7. Saleh, A. A. E. & Dionne, J. A. Toward efficient optical trapping of sub-10-nm particles with coaxial plasmonic apertures. *Nano Lett.* **12**, 5581–5586 (2012).
8. Zheng, Y. et al. Nano-optical conveyor belt, part II: demonstration of handoff between near-field optical traps. *Nano Lett.* **14**, 2971–2976 (2014).
9. Roxworthy, B. J. et al. Application of plasmonic bowtie nanoantenna arrays for optical trapping, stacking, and sorting. *Nano Lett.* **12**, 796–801 (2012).

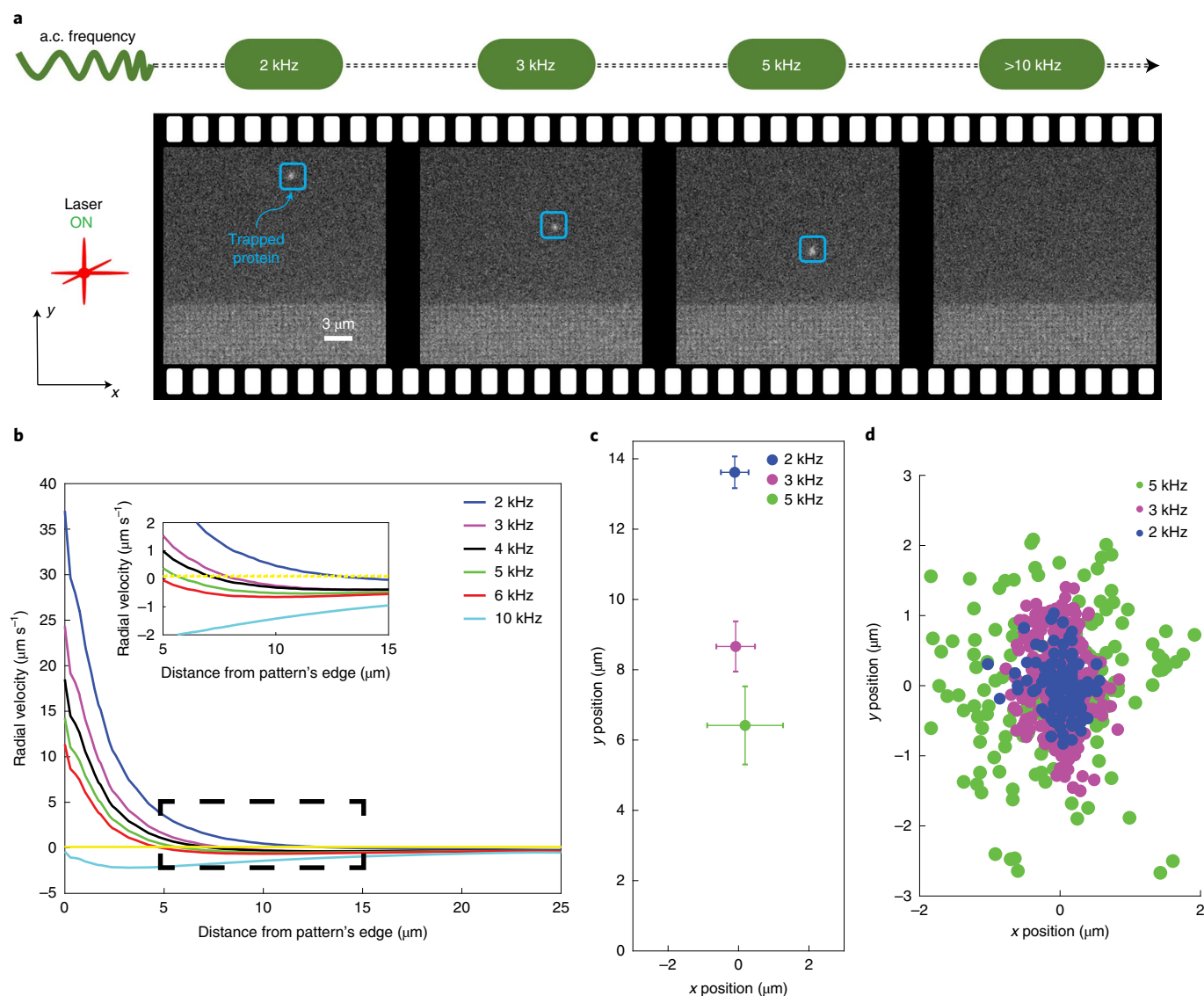


Fig. 4 | Illustration of trapping stability and trapping position as a function of a.c. frequency. **a**, Frame-by-frame demonstration of the trapped molecule's position under different a.c. frequencies. Under 2 kHz a.c. frequency, the single molecule is trapped farther away from the pattern's edge. When the a.c. frequency is tuned higher, from 2 kHz to 5 kHz, the trapping position is shifted inward, closer to the pattern's edge. **b**, Simulated radial velocity under different a.c. frequencies along the direction perpendicular to the length of the pattern, following the dashed line in Fig. 1d. Inset of Fig. 4b indicates the zoomed-in version corresponding to the black dashed box. Positive radial velocity means velocity directed away from the nanohole array, while negative velocity means velocity directed inward. The position of the stagnation zone (that is, where the velocity goes to zero) is dependent on the a.c. frequency. This behaviour arises because the a.c. electro-osmotic flow is dependent on the zeta potential, which varies with the a.c. frequency, as depicted in Supplementary Figs. 1 and 2. **c**, Mean distance of single molecule under each a.c. frequency. The pattern's edge is defined as the y position = 0, while $x = 0$ is defined as the mean x position of the single molecule. Error bars represent the standard deviation for each a.c. frequency along either the x or y direction. **d**, Scatter plot of tracked BSA molecule position under different a.c. frequencies. The result shows that the trapping stability is higher at lower a.c. field frequencies.

10. Lin, L. et al. Opto-thermoelectric nanotweezers. *Nat. Photon.* **12**, 195–201 (2018).

11. Mandai, S., Serey, X. & Erickson, D. Nanomanipulation using silicon photonic crystal resonators. *Nano Lett.* **10**, 99–104 (2010).

12. Wang, K., Schonbrun, E., Steinvurzel, P. & Crozier, K. B. Trapping and rotating nanoparticles using a plasmonic nano-tweezer with an integrated heat sink. *Nat. Commun.* **2**, 469 (2011).

13. Shoji, T. & Tsuboi, Y. Plasmonic optical tweezers toward molecular manipulation: tailoring plasmonic nanostructure, light source, and resonant trapping. *J. Phys. Chem. Lett.* **5**, 2957–2967 (2014).

14. Ndukaife, J. C. et al. Long-range and rapid transport of individual nano-objects by a hybrid electrothermoplasmonic nanotweezer. *Nat. Nanotechnol.* **11**, 53–59 (2016).

15. Ndukaife, J. C. et al. High-resolution large-ensemble nanoparticle trapping with multifunctional thermoplasmonic nanohole metasurface. *ACS Nano* **12**, 5376–5384 (2018).

16. Ndukaife, J. C., Shalae, V. M. & Boltasseva, A. Plasmonics—turning loss into gain. *Science* **351**, 334–335 (2016).

17. Garcia-Guirado, J. et al. Overcoming diffusion-limited biosensing by electrothermoplasmonics. *ACS Photonics* **5**, 3673–3679 (2018).

18. Hong, C., Yang, S. & Ndukaife, J. C. Optofluidic control using plasmonic TiN bowtie nanoantenna. *Opt. Mater. Express* **9**, 953–964 (2019).

19. Dienerowitz, M., Mazilu, M., Reece, P. J., Krauss, T. F. & Dholakia, K. Optical vortex trap for resonant confinement of metal nanoparticles. *Opt. Express* **16**, 4991–4999 (2008).

20. Fränzl, M. et al. Thermophoretic trap for single amyloid fibril and protein aggregation studies. *Nat. Methods* **16**, 611–614 (2019).

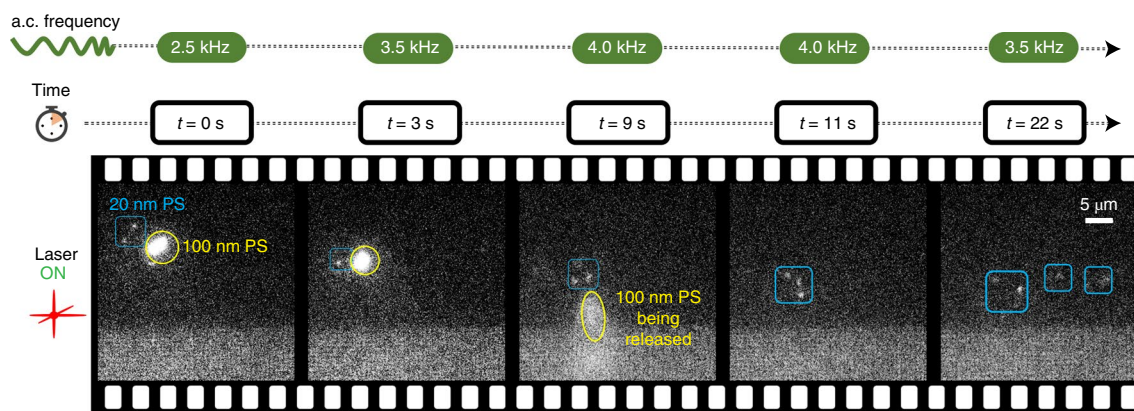


Fig. 5 | Frame-by-frame sequence showing the size-based sorting of dielectric polystyrene beads using OTET. The 20 nm polystyrene beads (PS) are highlighted in blue rectangles, and the 100 nm bead is inside the yellow circle, and is much brighter. Initially, the a.c. frequency is set as 2.5 kHz. Both 20 nm and 100 nm polystyrene beads are trapped near the edge of the nanohole array. After 3 s, the a.c. frequency is tuned to 3.5 kHz so that all the beads move closer to the pattern. When the a.c. frequency is increased to 4 kHz, the 100 nm bead becomes unstable and is sorted out, while the 20 nm beads remain trapped. The first four frames demonstrate the sorting process chronologically. To ensure that the 20 nm beads are stably trapped, the a.c. frequency is tuned down to 3.5 kHz again, and they remain trapped.

21. Squires, T. M. & Bazant, M. Z. Induced-charge electro-osmosis. *J. Fluid Mech.* **509**, 217–252 (2004).
22. Melcher, J. R. & Firebaugh, M. S. Traveling-wave bulk electroconvection induced across a temperature gradient. *Phys. Fluids* **10**, 1178–1185 (1967).
23. Hatlo, M. M. & Lue, L. The role of image charges in the interactions between colloidal particles. *Soft Matter* **4**, 1582–1596 (2008).
24. Nagpal, P., Lindquist, N. C., Oh, S. H. & Norris, D. J. Ultrasmooth patterned metals for plasmonics and metamaterials. *Science* **325**, 594–597 (2009).
25. Ghosh, S. & Ghosh, A. All optical dynamic nanomanipulation with active colloidal tweezers. *Nat. Commun.* **10**, 4191 (2019).
26. Pang, Y. & Gordon, R. Optical trapping of a single protein. *Nano Lett.* **12**, 402–406 (2012).
27. Krishnan, M., Mojarad, N., Kukura, P. & Sandoghdar, V. Geometry-induced electrostatic trapping of nanometric objects in a fluid. *Nature* **467**, 692–695 (2010).

Publisher's note Springer Nature remains neutral with regard to jurisdictional claims in published maps and institutional affiliations.

© The Author(s), under exclusive licence to Springer Nature Limited 2020

Methods

Device fabrication. A 5-nm-thick Cr mask was deposited on a 1.5 mm × 1.5 mm silicon wafer using a resistive evaporator. Subsequently, the substrate was spin-coated with 400 nm ZEP-520A photoresist and baked at 180 °C for 2 min. Electron-beam lithography was used to pattern the nanohole arrays to produce a nanohole radius of 150 nm and a lattice constant of 590 nm. The dimension of the square array pattern is 70 μm. The patterned resist was developed in ZED N50 for 2 min, rinsed with isopropyl alcohol and blown dry in nitrogen. After 7 s of descumming, Cl₂ plasma etching was applied for 75 s to transfer the pattern onto the Cr layer serving as the hard mask for a subsequent reactive ion etching process. Reactive ion etching proceeded for 2 min to open ~200-nm-deep nanoholes into the silicon wafer. To ensure the whole photoresist and Cr mask layers were stripped off before depositing the gold film, the patterned silicon wafer was sonicated in acetone for 10 min, then soaked in Cr etchant for 10 min. At this point, the patterned silicon wafer became a template. Subsequently, 120 nm gold film was deposited on the template. The resistive evaporator was again used to deposit a 120-nm-thick gold film onto the template. We then applied UV-curable epoxy onto the gold film, covered it with a glass substrate that has a thin coating of indium tin oxide and exposed it under UV light (324 nm wavelength) for 12 min to harden the epoxy. After we peeled the gold film off the Si template, we packed the gold film into a microfluidic channel. The used Si template was cleaned using O₂ plasma etching and gold etchant. We reused the Si template by easily depositing another 120-nm-thick gold film and performing the template stripping process again.

Sample preparation. To package the gold nanohole array sample into a microfluidic chip, we treated the surface of the gold film using a polymer solution for 10 min to ensure that the surface acquired a net surface charge to prevent particles from sticking to the surface. The polymer solution consisted of poly (sodium 4-styrenesulfonate) potassium chloride (1:5) solution in water (1:25). Then the sample was thoroughly flushed under deionized water and blown dry under N₂. Finally, we sandwiched the gold film by covering it with another glass cover-slip that has a thin coating of indium tin oxide, spaced by a 120-μm-thick dielectric spacer to create a microfluidic channel around the patterns.

The BSA or polystyrene beads were originally of a concentration of 1 mg ml⁻¹. The BSA is fluorescently labelled with tetramethylrhodamine dyes that absorb at 532 nm and emit at about 600 nm. The fluorescently labelled BSA molecules were purchased from Thermo Fisher Scientific. The BSA was diluted by one billion times using deionized water to generate a sparse enough solution suitable for single-molecule manipulation. The final concentration of the BSA molecules used in the experiment was 15 fM. The solution of 20 nm polystyrene beads was diluted by ten million times, while the solution of 100 nm polystyrene beads was diluted by one million times.

Fluorescence imaging. The trapping and imaging was performed using a custom fluorescent imaging and optical trapping microscope based on a Nikon Ti2-E inverted microscope. The suspended particle solution was injected into the microfluidic channel. A high quantum efficiency sCMOS camera (Photometrics PRIME 95B) was used to acquire images at a frame rate of 2.5 frames per second. The trapped fluorescent polystyrene beads were excited under green light from a filtered broadband fluorescent illumination lamp (Nikon INTENSILIGHT C-HGFI). The emitted red light was collected through the same objective lens and imaged on the camera. The nanohole array was excited with a 973 nm semiconductor diode laser (Thorlabs CLD1015). The laser beam was focused with a Nikon ×60 water-immersion objective lens (NA, 1.2). The a.c. electric field was supplied by a dual-channel function generator (BK Precision 4047B).

Electrical conductivity measurements. Electrical conductivity and electrophoretic mobility were measured using a Litesizer 500 (Anton Paar). The electrical conductivity of the BSA protein sample was 3.3 mS m⁻¹, while its electrophoretic mobility was -3 μm cm V⁻¹ s⁻¹.

Multiphysics simulations. The electromagnetic simulation was performed using a full-wave simulation formalism in Lumerical finite-difference time-domain software. A periodic boundary condition with a 590 nm lattice constant was applied to mimic an infinite array of nanoholes. Perfectly matched layers were placed at the top and bottom of the domain to prevent backscatter from the boundaries. A linearly polarized plane wave served as the light source. Absorption was calculated by 1 - R - T, where R was the reflectance and T was the transmittance solved. A three-dimensional COMSOL model was established to solve the heat transfer and fluid dynamics problem. A prescribed temperature of 293.15 K was set at the boundaries for solving the heat transfer physics. The a.c. electro-osmosis flow was modelled using a slip boundary condition on the surface of the nanohole array. The slip velocity is the electro-osmotic slip velocity \bar{u} given by $\bar{u} = \mu_{eo} \bar{E}_t$, where $\mu_{eo} = -\frac{\epsilon_0 \zeta}{\mu}$ is the electro-osmotic mobility and ϵ_0 is the relative permittivity; ζ is the zeta potential and μ is the dynamic viscosity of the liquid. $\bar{E}_t = \bar{E} - (\bar{E} \cdot \bar{n}) \bar{n}$, and \bar{E} is the electric field calculated by solving Poisson's equation, as described in the Supplementary Information. \bar{n} is the unit vector in the normal direction. The zeta potential used was calculated from the measured values, as described in the Supplementary Information. The no-slip boundary condition, which is $\bar{u} = 0$, was set on all other boundaries. The thermal properties of glass, gold and water were adapted from the COMSOL material library. The measured electrical conductivity of liquid was used. The relative permittivity of water was set as 78.

Data availability

The datasets generated and/or analysed during the current study are available in the Harvard Dataverse repository (<https://doi.org/10.7910/DVN/LFVQOD>). Source data are provided with this paper.

Acknowledgements

The authors acknowledge financial support from the National Science Foundation (NSF ECCS-1933109) and Vanderbilt University. We thank A. Locke for providing the protein samples and K. Wang and C. Batista for help with the zeta potential measurements.

Author contributions

J.C.N. conceived and guided the project. C.H. fabricated the samples and performed the experiments and the numerical simulations. S.Y. contributed to the wave-optics simulations. J.C.N. and C.H. discussed the results and wrote the manuscript.

Competing interests

The authors declare no competing interests.

Additional information

Supplementary information is available for this paper at <https://doi.org/10.1038/s41565-020-0760-z>.

Correspondence and requests for materials should be addressed to J.C.N.

Peer review information *Nature Nanotechnology* thanks Reuven Gordon and the other, anonymous, reviewer(s) for their contribution to the peer review of this work

Reprints and permissions information is available at www.nature.com/reprints.